RESEARCH ARTICLE

NANO · MICRO small
www.small-journal.com

Direct Synthesis of CuPd Icosahedra Supercrystals Studied by In Situ X-Ray Scattering

Davide Derelli, Kilian Frank, Lukas Grote, Federica Mancini, Ann-Christin Dippel, Olof Gutowski, Bert Nickel, and Dorota Koziej**

Nanocrystal self-assembly into supercrystals provides a versatile platform for creating novel materials and devices with tailored properties. While common self-assembly strategies imply the use of purified nanoparticles after synthesis, conversion of chemical precursors directly into nanocrystals and then supercrystals in simple procedures has been rarely reported. Here, the nucleation and growth of CuPd icosahedra and their consecutive assembly into large closed-packed face-centered cubic (fcc) supercrystals are studied. To this end, the study simultaneously and in situ measures X-ray total scattering with pair distribution function analysis (TS-PDF) and small-angle X-ray scattering (SAXS). It is found that the supercrystals' formation is preceded by an intermediate dense phase of nanocrystals displaying short-range order (SRO). It is further shown that the organization of oleic acid/oleylamine surfactants into lamellar structures likely drives the emergence of the SRO phase and later of the supercrystals by reducing the volume accessible to particle diffusion. The supercrystals' formation as well as their disassembly are triggered by temperature. The study demonstrates that ordering of solvent molecules can be crucial in the direct synthesis of supercrystals. The study also provides a general approach to investigate novel preparation routes of supercrystals in situ and across several length scales via X-ray scattering.

1. Introduction

The production of hierarchically structured materials is driving many recent advances in the fields of photonics,[1] electronics,[2] catalysis,[3] sensing,[4] and nanomedicine.[5] The self-assembly of nanocrystals into crystalline lattices constitutes a promising bottom-up route to such metamaterials, as it permits to tune the functional emergent properties of the outcoming supercrystals via engineering of the individual building blocks.[6] While recent improvements in the field of colloidal synthesis provide a high level of control of nanocrystal size, shape, and composition,[7] most synthetic schemes do not directly deliver supercrystals. Self-assembly procedures typically require several purification steps of the nanocrystal product and further rely on slow solvent evaporation or destabilization of the nanocrystal dispersion over a time up to many hours or days.[6e,8] Only few reports demonstrate the direct conversion of molecular precursors into supercrystals via a one-pot strategy.[9] In these studies, the formation of the ordered superstructures is primarily ascribed to the attractive van der Waals forces affecting the nanocrystal cores, balanced by the steric repulsion of the organic surface ligands.[10] Moreover, the mixtures of different ligands determine the degree of crystallinity and the symmetry of Pd-based supercrystals.[9b] Yet, the dynamical processes governing the concerted nanocrystal synthesis and supercrystal formation remain underexplored. For instance, the role of the solvent molecules and ligand shells[11] and the existence of intermediate states due to potential

D. Derelli, L. Grote, F. Mancini, D. Koziej
Institute for Nanostructure and Solid-State Physics
Center for Hybrid Nanostructures
University of Hamburg
22761 Hamburg, Germany
E-mail: dorota.koziej@uni-hamburg.de

K. Frank, B. Nickel
Faculty of Physics and Center for NanoScience (CeNS)
Ludwig-Maximilians-Universität München
80539 Munich, Germany
E-mail: bert.nickel@lmu.de

A.-C. Dippel, O. Gutowski
Deutsches Elektronen-Synchrotron DESY
22607 Hamburg, Germany

D. Koziej
The Hamburg Centre for Ultrafast Imaging
22761 Hamburg, Germany

F. Mancini
Current affiliation: National Research Council of Italy
Institute of Science, Technology and Sustainability for Ceramics
CNR - ISSMC (former ISTEC), 64 I-48018 Via Granarolo, FAENZA (RA), Italy

The ORCID identification number(s) for the author(s) of this article can be found under https://doi.org/10.1002/smll.202311714

DOI: 10.1002/smll.202311714

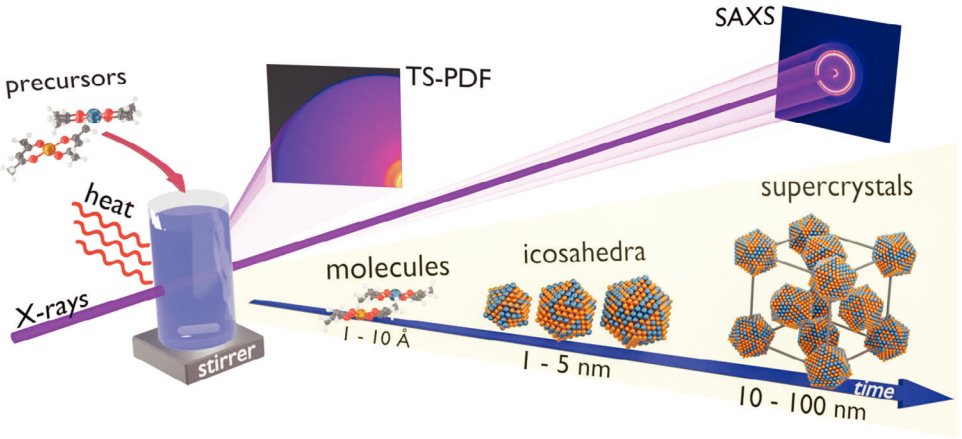

Figure 1. Schematic illustration of the simultaneous in situ TS-PDF and SAXS experiment and overview of the main findings. A reaction mixture containing the Cu and Pd precursors is stirred during temperature ramps. The X-ray TS and SAXS signal of the reaction mixture is recorded simultaneously by two large-area detectors. Metallic CuPd icosahedra nucleate from the molecular precursors and subsequently assemble into colloidal supercrystals with a fcc arrangement.

non-classical crystallization pathways[6d,12] for the supercrystals are still largely unknown.

Here, we use high energy X-ray scattering techniques to obtain insights into the nanocrystal formation and assembly over multiple length scales. In situ X-ray scattering has proven to be an outstanding method to probe nanoparticle formation[13] and self-assembly processes.[9a,14] The simultaneous measurement of X-ray total scattering with pair distribution function analysis (TS-PDF) and small-angle X-ray scattering (SAXS) in a single experimental setup enables us to observe both the nucleation of CuPd icosahedra and their subsequent arrangement into close-packed supercrystals, as summarized in **Figure 1**. Our study reveals that the solvent molecules, particularly oleylamine and oleic acid, play a double role in the synthetic and assembly steps. During synthesis at elevated temperatures, they create a soft organic shell that envelops the metallic icosahedral cores and prevent aggregation and fusion of the nanocrystals within the isotropic solvent. Upon cooling to lower temperatures, solvent molecules arrange into a lamellar phase which induces the nanocrystals' self-assembly. First, nanocrystals assemble in a dense short-range ordered (SRO) phase, then the supercrystals emerge. The structuring of the solvent molecules effectively promotes the assembly process by reducing the accessible volume to particle diffusion. We therefore identify a generic mechanism for the one-pot formation of supercrystals mainly driven by entropic forces.

2. Results and Discussion

We synthesize CuPd nanocrystals by heating copper and palladium acetylacetonate precursor in a solvent mixture consisting of oleylamine, oleic acid, and dioctyl ether to 220 °C at 10 °C/min. The details of the in situ experimental setup are shown in Figures S1 and S2 (Supporting Information).[15] **Figure 2** exhibits the in situ TS-PDF and SAXS data collected simultaneously during the colloidal synthesis. In the background subtracted TS data, broad diffraction peaks appear within two minutes after reaching 220 °C, indicating the fast formation of small nanocrystals (Figure S3, Supporting Information). We Fourier transform the TS signal to obtain the pair distribution function G(r) shown in Figure 2b,d and Figures S4 and S5 (Supporting Information). At room temperature, the PDF exhibits an intense peak at 2.01 $Å^{-1}$. This distance is significantly longer than the metal-oxygen bond length in the Cu or Pd acetylacetonate precursors and hints at the formation of amine coordinated complexes of Cu^{2+} and Pd^{2+} cations upon dissolution, in agreement with previous reports.[16] Upon heating of the reaction mixture, the evolution of the PDF indicates a rapid nucleation and growth of CuPd nanocrystals of ≈3 nm in size. After 5 min at elevated temperature, no further changes are observed in the PDF, suggesting that the nanocrystal synthesis is completed. At low temperatures, the complementary SAXS data in Figure 2c,e displays a broad peak at 0.24 $Å^{-1}$ which stems from the metallic complexes in solution. About 95 s after reaching the reaction temperature of 220 °C, we observe a dramatic increase in the intensity at low scattering vector q, which identifies the emergence of nanometer-sized particles followed by particle growth, in line with the PDF analysis.

2.1. Atomic Structure of the Inorganic Nanocrystal Cores

We analyze the PDF signal at a late stage of the synthesis (t = 10 min) to determine the atomic structure and dimensions of the inorganic nanocrystals. We first model the PDF data by means of the well-established attenuated crystal (AC) approximation, which assumes the nanocrystals are single-crystalline spheres. However, this model provides a poor fit to the experimental data, both in the case of bulk CuPd alloys (space group Fm-3m, Figure S6a,b, Supporting Information) and cubic or tetragonal intermetallic phases (space group Pm-3m and P4/mmm respectively, Figure S6c,d, Supporting Information).

To capture the structural features encoded in the PDF, we clearly need to extend the candidate structures beyond single-crystalline, spherical models. We thus generate many discrete atomic models of various sizes and atomic arrangements, and we then test them individually against the experimental PDF. This approach is referred to as cluster mining and was recently

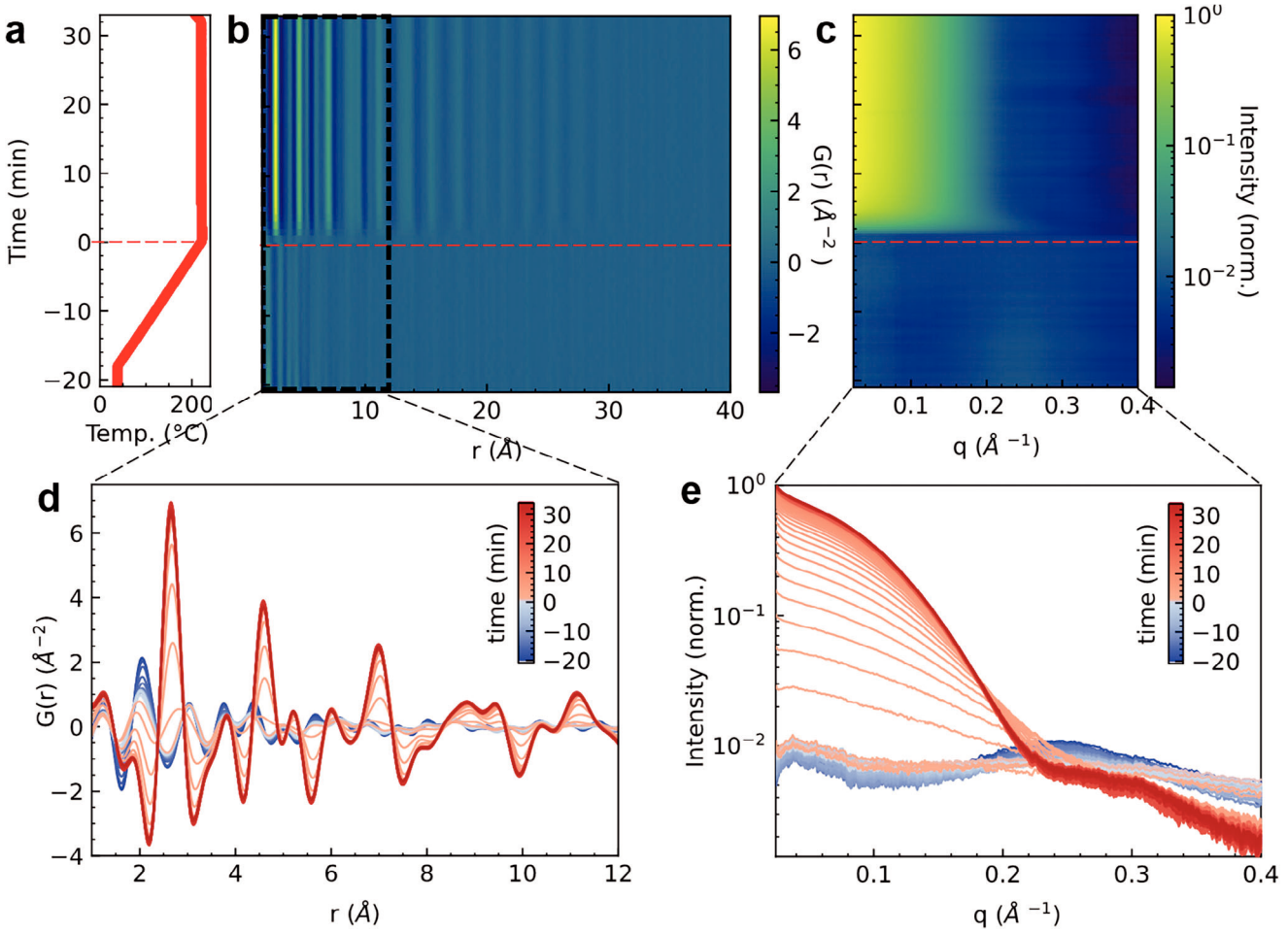

Figure 2. Simultaneous in situ PDF and SAXS during CuPd nanocrystal formation. a) Temperature profile during the synthesis of CuPd nanocrystals. At time = 0 min the reaction temperature of 220 °C is reached. b) 2D plot of the PDF as a function of time. The signal of the empty in situ reactor was subtracted as a background. The corresponding 1D plots are shown in (d). c) 2D plot of the SAXS intensity as a function of time. The corresponding 1D plots are shown in (e).

established for the PDF analysis of monometallic nanocrystal powders.[17] Here, we apply it for the first time to the analysis of in situ data, i.e., during synthesis. We consider various structural motifs displaying either single-crystalline domains (spheres, octahedra, and truncated octahedra), or fivefold twin boundaries (decahedrons and icosahedrons). We build alloyed CuPd models by fixing the Cu:Pd atomic ratio to 60:40, as determined by transmission electron microscopy-with energy dispersive X-ray spectroscopy (TEM-EDX) measurements on the final nanocrystals (Figure S7, Supporting Information).

We quantify the goodness-of-fit provided by each cluster model by means of weighted residual error (R_w) values, which we summarize in **Figures** 3a and S8 (Supporting Information). The best fit for each structural motif is shown in Figure 3b,c and Figure S9 (Supporting Information). The decahedral model provides an excellent fit at short atomic pair distances, but at longer distances results in weak, non-random oscillations in the differential curve, which indicate that the model does not fully capture the nanocrystal structure. It also predicts particles with a maximal axial size of 1.6 nm and a diameter of 2.1 nm, which are much smaller compared to the sizes revealed by TEM (Figure S10, Supporting Information). Conversely, the icosahedral model predicts nanocrystal sizes of 3.2 nm, in line with the TEM analysis. High-resolution transmission electron microscopy (HRTEM) measurements further evidence the presence of the twinned, icosahedral nanocrystals as synthetic products (Figure 3e,f; Figure S11, Supporting Information).[18]

An icosahedral nanocrystal is made up of 20 face-sharing tetrahedra displaying (face-centered cubic) fcc structure. Compared to the ideal model, we expect the CuPd nanocrystal sample to exhibit a certain degree of heterogeneity due to the presence of, e.g., point defects, interstitial atoms between the tetrahedral domains, size polydispersity, and inhomogeneous composition or distribution of the Cu and Pd atoms in the lattice. The summed contribution of all these structural defects results in very small, randomized deviations in the averaged atomic arrangement of the CuPd nanocrystals from the ideal icosahedral configuration and causes the discrepancy between the experimental and simulated PDF in Figure S9d (Supporting Information). We test this hypothesis by a Monte Carlo sampling procedure, which allows minor atomic displacements in the model structure. The relaxed model perfectly fits the experimental PDF, as shown in Figure 3d,

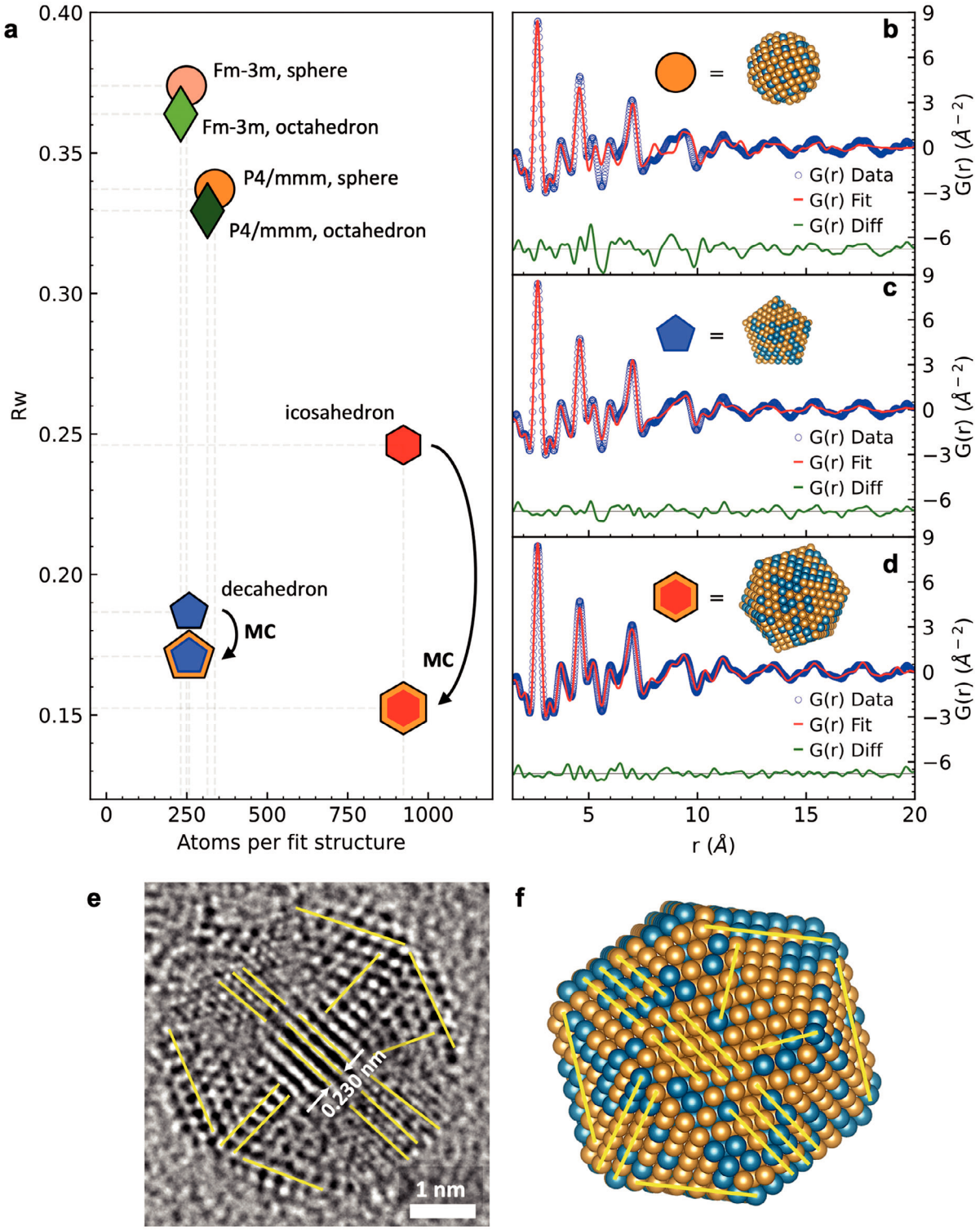

Figure 3. Determination of the nanocrystal core structure by PDF and HRTEM. a) Scatter plot of the weighted residual error (R_w) obtained by fitting the PDF of the final product by discrete atomistic models. The plot displays the best-fitting structures per each of the considered structural motifs. A yellow frame outlines the fit structures obtained by using a Monte Carlo (MC) routine. b–d) PDF fits for selected structural motifs from a. Blue circles represent experimental data, red lines the fits, and green lines the residual between experimental and fit PDFs. In the insets, the structural model relative to each fit is shown. e,f) An HRTEM image of a CuPd nanocrystal (e) is compared to an icosahedral cluster model (f). Yellow lines are guides to the eye underlining the major structural motifs for both.

while overall retaining the icosahedral arrangement, see Figure S12 (Supporting Information). The application of the same routine to the decahedral model does not significantly improve the fit (Figure S13, Supporting Information). We therefore conclude that the CuPd nanocrystal is best described by the icosahedral arrangement, as consistently supported by both EM analysis and PDF results.

2.2. Evolution of the Nanocrystals during Synthesis

The analysis of the in situ PDF and SAXS data permits to extract quantitative information from the nucleation and growth of the CuPd icosahedra. As the nanocrystals grow, the amplitude of the PDF oscillations increases and the structural features extend to longer interatomic distances, as shown in **Figures** 4a and S14 (Supporting Information). We fit the time-dependent in situ PDF by a series of CuPd icosahedral models of different sizes, which consist of a varying number of discrete atomic shells N_{shells}. In addition, we fit the in situ SAXS intensities by a form factor model of moderately polydisperse spheres, as shown in Figure 4b.

The particle diameters determined by the two techniques follow a similar trend throughout the reaction time, see Figure 4c. The particle diameter revealed by SAXS increases smoothly whereas PDF analysis results in a stepwise increase of the nanocrystal sizes due to the discrete number of shells in the icosahedral models. While the PDF signal mainly originates from interatomic distances limited to the nanocrystal inorganic cores, SAXS intensities are also partly sensitive to the presence of a soft shell of organic ligands surrounding the nanocrystal surface. Since the shell consists of highly packed organic molecules, it displays a higher electron density compared with the bulk isotropic solvent. Modeling the SAXS signal via a simple sphere model thus systematically overestimates the particle diameters compared with the PDF values. When we model the colloidal nanocrystals as high-scattering contrast cores surrounded by a decaying scattering contrast shell, the core sizes provided by SAXS and PDF analysis closely agree (Figure S15 and Table S1, Supporting Information). Fourier-transformed infrared spectroscopy (FTIR, Figure S16, Supporting Information) further confirms the presence of an organic shell of oleylamine and oleic acid ligands surrounding the CuPd nanocrystal cores.[19]

After ≈5 min at 220 °C, the formation of the CuPd icosahedra is completed, and the scale factor of the PDF fit reaches a plateau, as shown in Figure 4d. At this stage, the nanocrystal polydispersity is constant at 13.5%. An overview on nucleation and growth of CuPd icosahedra, combining the findings from the simultaneous in situ PDF and SAXS analysis is given in Figure 4e.

2.3. Directed Self-Assembly of CuPd Icosahedra

We direct the self-assembly of CuPd icosahedra into supercrystals by lowering the reaction temperature after synthesis and we monitor the process by in situ SAXS. **Figure** 5a displays representative 1D SAXS patterns acquired at different times during the cooling of the reaction mixture. Directly after synthesis and at high temperature, the form factor of the freely dispersed nanocrystals dominates the SAXS signal. Upon cooling, we observe the gradual emergence of intense diffraction peaks, which indicate the formation of a crystalline superlattice with a close-packed fcc arrangement and a lattice constant of 10.24 nm (Figure 5a; Figure S17, Supporting Information).

Before supercrystal formation, we observe the appearance of peaks in the SAXS intensity at 0.16 and 0.32 $Å^{-1}$ which indicate the emergence of a lamellar phase with a repeating unit size of 3.9 nm, as shown in Figure 5a and Figures S17 and S18 (Supporting Information). The size is characteristic of bilayer structures of oleic acid/oleylamine solvent molecules.[20] Furthermore, we observe the presence of a short-range ordered (SRO) phase of CuPd nanocrystals with a typical interparticle distance of ca. 8–9 nm, i.e., wider than the nanocrystal core diameter (3.2 nm) plus a shell of fully extended oleic acid/oleylamine molecules (4 nm).

We calculate the Porod invariant Q from the SAXS intensity (see Experimental Section) for each of the four phases (free particles, solvent lamellae, SRO phase, and supercrystals) to quantify their respective volume fractions during cooling of the reaction mixture. The time-resolved evolution of the Porod invariants is reported in Figure 5b. The formation of the solvent lamellae during the cooling ramp starts at ≈130 °C and is immediately followed by the slow emergence of the SRO phase. Extended annealing at 100 °C for 30 min promotes a continuous growth of the SRO phase and eventually the formation of the supercrystals. The supercrystal nucleation occurs homogeneously within the solvent, as revealed by the isotropic diffraction rings in the SAXS pattern shown in the inset of Figure 5a. After nucleation, the supercrystals rapidly grow above 100 nm in only 15 min, see Figure S19 (Supporting Information). We therefore detect an assembly process that is much faster than common self-assembly procedures of colloidal nanocrystals.

2.4. Mechanism of the Supercrystal Formation

Increasing the particle density by, e.g., solvent evaporation is a common strategy to induce the assembly of colloidal crystals.[6e,21] In freezing-induced self-assembly methods, the crystallization of the solvent and the subsequent expulsion and aggregation of solutes constitute the driving force of the assembly process.[22] Here, we show that cooling of the surfactant-rich reaction mixture induces the formation of solvent lamellae, which in turn promotes the emergence of the SRO phase and finally of the supercrystals. Additionally, Figure S20 (Supporting Information) shows the SAXS data after heating up and then cooling down the solvent mixture in the absence of the Cu and Pd precursors. During the process, we observe the formation of lamellae with a repeating unit size of 3.84 nm, i.e., very close to the one determined in the presence of the nanocrystals. This result suggests that the organization of the solvent molecules into the lamellar phase coincides with a simultaneous segregation of the nanocrystals, which accumulate into particle-dense subphases. We thus observe the emergence of a particle-dense SRO phase. As the solvent lamellae rearrange over time, a growing number of nanocrystals segregate from the lamellar phase into a restricted environment. We accordingly determine a decrease in the fraction of freely dispersed nanocrystals. During the process, the typical interparticle distance of the SRO phase progressively reduces from 9.2 nm to 8.1 nm, as shown in Figure S21 (Supporting Information). The SRO finally evolves into the fcc arrangement,

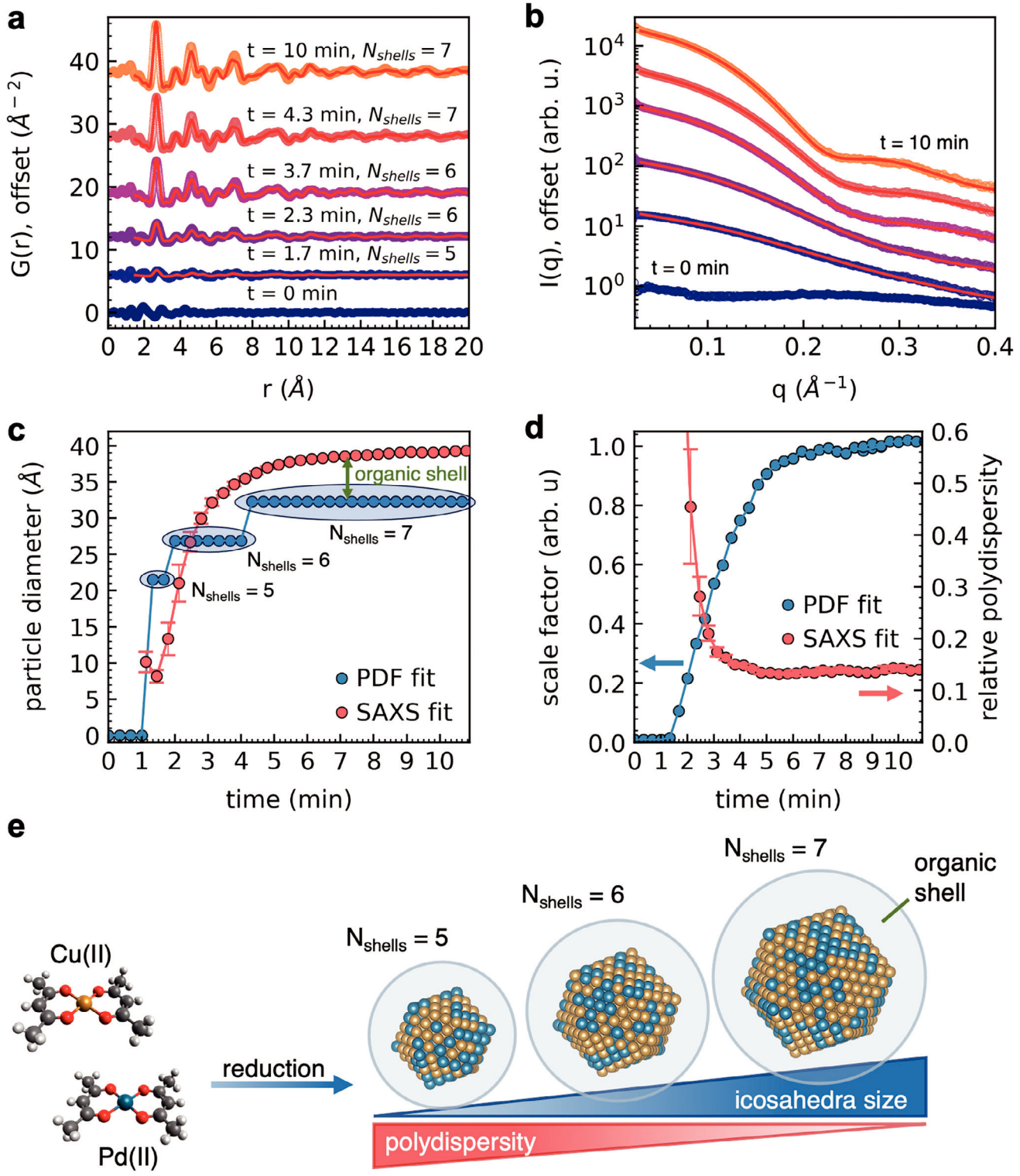

Figure 4. CuPd nanocrystal nucleation and growth. a) PDF data measured at selected times during the nanocrystal formation. Red lines indicate the fit of the experimental data with an icosahedral model characterized by a discrete number of atomic shells (N_{shells}). b) SAXS intensities at the same selected times as in (a). c) Particle diameter as a function of time as obtained by fit of PDF and SAXS data. The larger diameters predicted by SAXS stem from the presence of a soft organic shell surrounding the nanocrystals. d) Scale factor and relative polydispersity as determined by the fit of PDF and SAXS data, respectively. The data points and error bars for SAXS fits in (c) and (d) represent the mean values and standard deviations obtained from four consecutive SAXS intensity curves. e) Schematic illustration of the growth process of colloidal CuPd icosahedra.

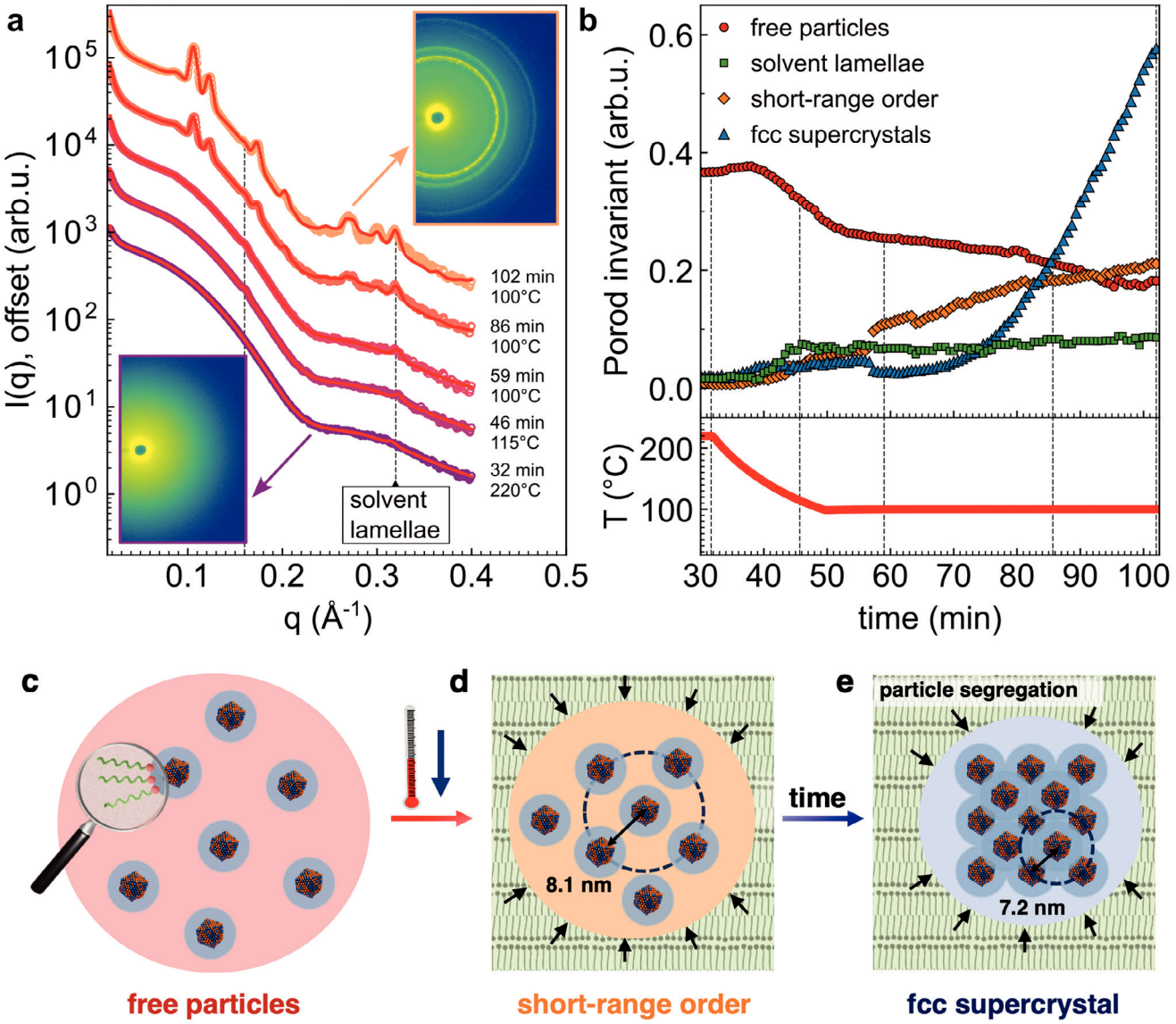

Figure 5. Formation of the supercrystals. a) SAXS profiles at selected time points before, during, and after formation of the supercrystals. Red lines indicate the fit of the experimental data. Dashed black lines indicate the position of the peaks originating from solvent lamellae. In the insets, the detector images corresponding to the first and last profiles are shown. b) Time-resolved plot of the Porod invariants, which quantify the contribution of the free particles, solvent lamellae, short-range ordered particles, and fcc supercrystals to the SAXS intensity over time. The temperature profile during the cooling of the reaction mixture and subsequent thermal treatment at 100 °C after the nanocrystal synthesis is additionally shown. At time = 0 min the reaction temperature of 220 °C was first reached (data shown in Figure 2). c–e) Schematic illustration of the formation mechanism of the supercrystals. Cooling of the reaction mixture induces the freely dispersed particles (c) to arrange into the short-range ordered phase (d) due to the emergence of solvent lamellae and the subsequent formation of particle-dense subphases. Over time, the short-range ordered phase further evolves into supercrystals of fcc arrangement and of shorter interparticle distance (e).

which allows to maximize the nanocrystals packing density in the reduced volume. We therefore conclude that the supercrystals' nucleation occurs via a two-step process in which the formation of an amorphous dense phase precedes the nanocrystal crystallization.[6d,12a] The overall self-assembly mechanism is illustrated in Figure 5c–e.

Previous studies suggest that a competition of long-ranged van der Waals attractive forces and short-ranged steric repulsion is crucial for the direct synthesis of colloidal supercrystals. In the presence of core-core attraction, the soft shells stabilizing adjacent nanocrystals in the superlattice partially interpenetrate, resulting in a shorter surface-to-surface separation than the thickness of the two shells. For example, a 1.95 nm separation was observed for superlattices of 6 nm Pd nanocrystals capped with oleic acid, and a 3 nm separation is predicted for identical particles of 3 nm in size at 503K.[9b] However, in this work we find a larger surface-to-surface separation within the supercrystals of 4 nm (see Experimental Section) corresponding to twice the length of a fully extended oleylamine/oleic acid molecule. The result indicates that no interpenetration of the organic shells between

adjacent nanocrystals is present. Moreover, it suggests that attractive forces between the metal cores are rather weak.

We confirm our observation by calculating the effect of the van der Waals attraction and steric repulsion between 3 nm CuPd nanocrystals in presence of surface ligands. In Figure S22 (Supporting Information), the resulting pair-wise potential displays a very shallow minimum located at a 3.9 nm surface-to-surface separation of –0.02 k_BT, i.e., much smaller than the kinetic energy of the nanocrystals. We therefore conclude that long-ranged van der Waals attraction alone is too weak to drive freely dispersed nanocrystals to assemble. Instead, we propose that the lamellar formation and the subsequent nanocrystal segregation likely act as an initiator of the self-assembly process by limiting the available volume to nanocrystal diffusion. At increased particle density, the crystallization of CuPd icosahedra leads to an overall increase in the total entropy of the system, in analogy to hard spheres.[23] In fact, diluting a dispersion of the supercrystals at room temperature with either polar or apolar solvents leads to the immediate disruption of the crystalline order due to a decrease of the local particle volume fraction, as shown by SAXS in Figure S23 (Supporting Information). Although the result does not exclude the existence of short-range attractive forces, such as core-core or ligand-ligand interactions, within the supercrystals, it nevertheless indicates that these interactions are rather weak, even at short interparticle distances. We therefore conclude that interparticle attractions play only a minor role in the observed assembly process.

We demonstrate that the supercrystals disassemble and subsequently re-assemble upon increasing and then decreasing the temperature of the dispersion between 200 and 110 °C, as shown in Figure S24 (Supporting Information). During the heating, the supercrystals melt first while decomposition of the SRO phase unfolds at higher temperatures. Upon cooling, the emergence of the SRO phase precedes the supercrystal formation, as observed before. In situ PDF shows that the structure of the icosahedral inorganic cores is unaffected by both the melting and re-assembly, as evidenced in Figure S25 (Supporting Information).

In **Figure 6** we offer a schematic illustration of the direct synthesis and assembly of CuPd icosahedra, as determined by simultaneous in situ PDF and SAXS.

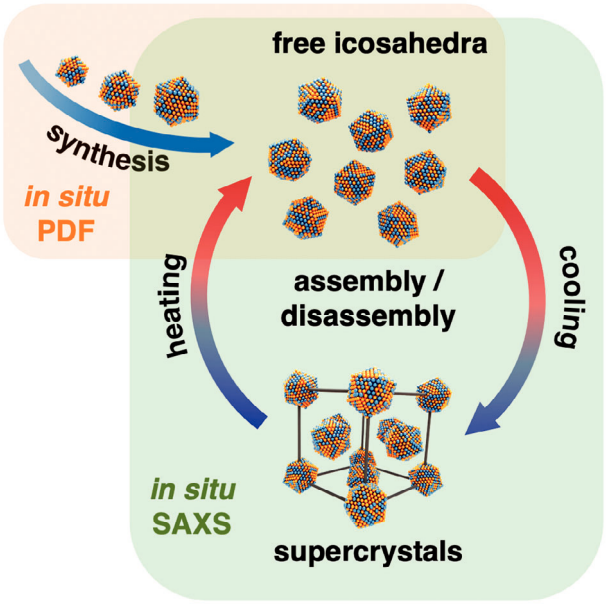

Figure 6. Schematic illustration of the synthesis of CuPd icosahedra and of the temperature-mediated melting and recrystallization of the supercrystals.

3. Conclusion

In summary, we determine the mechanisms leading to the direct synthesis and assembly of CuPd icosahedra into supercrystals in the presence of oleylamine and oleic acid. The simultaneous acquisition of in situ TS-PDF and SAXS allows us to follow the entire process from the atomic to the nanometer length scales. By in situ PDF, we obtain a precise description of the icosahedral structure of the metallic cores, which permits to track the growth of the nanocrystals and determine their size with a high degree of accuracy. During the formation of the icosahedra, oleylamine and oleic acid form a soft shell around the metallic cores that stabilizes the dispersion from aggregation. We show by in situ SAXS that upon cooling of the reaction mixture first a short-range ordered phase forms, which then converts into a crystalline fcc superlattice. We demonstrate that the assembly process is primarily driven by the organization of the oleylamine/oleic acid solvent molecules into lamellae which in turn induce the colloidal nanocrystals to segregate into dense subphases. The proposed mechanism contrasts with previous examples of one-pot synthesis and assembly of nanocrystals, in which the assembly process was predominantly attributed to van der Waals attraction and short-range steric repulsion. Finally, we show that the structure of the inorganic cores remains unaltered during the temperature-mediated melting and reassembly of the supercrystals.

This work identifies a new strategy toward the direct synthesis of colloidal supercrystals based on segregation of the as-formed nanocrystals from an ordering solvent. It also provides a general approach to investigate complex colloidal self-assembly processes by in situ scattering methods. While PDF provides a detailed description of the nanocrystal atomic arrangement, SAXS is ideally suited to probe periodic organizations at the nanoscale, such as nanocrystal dense phases, superlattices, and lamellar phases. The combined use of the two techniques thus constitutes a powerful tool to investigate in situ the preparation of hierarchically structured functional materials by novel and facile one-pot fabrication routes.

4. Experimental Section

Chemicals: Ethanol absolute (AnalR Normapur, VWR Chemicals), toluene (Emsure, Merk), copper acetylacetonate ($Cu(acac)_2$, >99.9% Sigma-Aldrich), palladium acetylacetonate ($Pd(acac)_2$, 99% Sigma-Aldrich), oleylamine (OAm, 99% Sigma-Aldrich), oleic acid (OAc, > 99.0%, TCI), dioctyl ether (Oct_2O, 99% Sigma-Aldrich), hexane (>99%, Sigma-Aldrich) were used as purchased without further purification.

Synthesis and Assembly of CuPd Nanocrystals: In a typical synthesis, a stock solution of the nanocrystal precursors was prepared in an argon-filled glovebox by dissolving $Pd(acac)_2$ (77.6 mg, 0.253 mmol) and $Cu(acac)_2$ (123.1 mg, 0.467 mmol) into a solvent mixture of OAm (3 mL), OAc (1 mL), and Oct_2O (0.8 mL). Around 80 µL of the precursor solution was subsequently transferred into a thin-walled borosilicate glass tube, which was sealed air-tight by use of a PEEK liner. The latter was

accommodated into the in situ reactor, which was heated up to the reaction temperature of 220 °C at a constant ramp of 10 °C min^{-1} and under stirring. At this temperature, the reaction mixture turned from blue to red, and finally to black, indicating the formation of nanocrystals. After 30 min at 220 °C, the cell was allowed to cool down naturally either directly to room temperature or to 100 °C to promote the formation of the supercrystals. After the synthesis, the nanocrystals were isolated from the reaction mixture after addition of ethanol (three times in volume) and by centrifugation. The nanocrystals were then washed at least three times by centrifugation after dispersion in one aliquot of toluene and subsequent addition of three aliquots of ethanol.

Material Characterization: The TEM and HRTEM imaging were carried out on a JEOL JEM-1011 operating at 100 kV and on a JEOL JEM-2200FS at 200 kV, respectively. EDX measurements were performed by using a Si(Li) JEOL JED-2300 detector equipped at the JEOL JEM 2200FS. FTIR spectra were recorded with a Bruker Alpha II spectrometer.

In Situ Reactor: The custom-made in situ reactor is illustrated in Figure S1 (Supporting Information). It consisted of a metallic body accommodating a sealed cylindrical liner. The metal body was equipped with a Pt100 temperature sensor (Honeywell) and two cartridge heaters (24 V, 100 W, Maxiwatt) for temperature control. PEEK (Bieglo) plates were used to improve the thermal insulation. The liner was made of PEEK (Bieglo) and permitted to air-tight seal a cylindrical borosilicate reaction vessel closed on one side (Hilgenberg, diameter 4.1 mm, wall thickness 0.05 mm). The reaction vessel was sealed air-tight within the liner by a PEEK sealing component and a FPM75 o-ring (Hug-Technik) pressed against the top side of the liner walls. Stirring of the reaction mixture was applied by use of a micro-stirrer (Variomag, Thermo Scientific) and a 2 mm magnetic bar (VWR) immersed in the solvent mixture.

Beamline Setup and Data Acquisition: Simultaneous in situ SAXS and TS measurements were performed at beamline P07 (second experimental hutch, EH2) at the PETRA III synchrotron facility at DESY, Germany by using a similar setup as shown in a previous publication.[15] The study used an X-ray beam of ≈103.2 keV and collected X-ray scattering signal at a frequency of 1 Hz by using two large-area 2D X-ray detectors (Varex XRD 4343CT and Dexela 1512) positioned at a distance of ≈0.77 and 4.66 m from the sample position, respectively. A helium-filled flight tube was used to reduce the background signal on the SAXS detector. Sample-to-detector distances were calibrated by use of LaB_6 and silver behenate powder standards packed into a 1 mm polyimide capillary (Detakta) and positioned at the center of the PEEK liner of the in situ cell. Determination of the background signal was performed after measurement of an empty borosilicate reaction vessel and of the reaction mixture, which was heated in situ and in the absence of the metal precursors. Instrumental parameters for the TS analysis were obtained after measurement of a silicon powder standard packed into one of the reaction vessels.

In-House SAXS Measurements: Laboratory SAXS data was recorded at the SAXS setup at the Soft Condensed Matter chair at LMU Munich. A Mo microfocus source ($\lambda = 0.71$ Å) was collimated to a beam size of ca. 1 × 1 mm (full width at half maximum). Data were recorded using a Pilatus3R 300K detector (Dectris) at 1 m sample-to-detector distance. Ex situ samples were accommodated the in situ reaction cell and measured for 1 h. The signal of an empty glass tube was used as a background.

Processing of TS-PDF Data: *pyFAI*[24] was used to calibrate and azimuthally integrate the 2D diffraction patterns into the 1D curves. Fourier transformation of the total scattering signal to the PDF was performed by using *PDFgetX3*[25] within the range $2.35 < q < 14.60$ $Å^{-1}$. The *DiffpyCMI*[26] Python library was used to calculate and fit the PDF both in the case of the attenuated crystal (AC) approximation as well as by use of the Debye scattering equation (DSE) calculated for discrete atomic models (cluster fit), similarly as reported in ref. [17]. Further details on the PDF fitting routine, as well as of the Monte Carlo optimization routine are reported in the Supporting Information. Discrete atomistic models were generated by using the Atomic Simulated Environment (ASE) Python library.[27]

Processing of SAXS Data: *pyFAI*[24] was used to calibrate and azimuthally integrate the SAXS data. SAXS intensities I(q) were then analyzed using *SasView* version 5.0.5[28] or by custom fit routines using the *lmfit* Python package.[29] The form factor of individual nanocrystals was fitted by using either a polydisperse spherical form factor or an "onion" form factor, accounting for a solid core and an exponentially decaying particle shell. The SRO phase was described by the Percus–Yevick structure factor of hard spheres. Porod invariants $Q = \int_0^\infty I(q)q^2dq = 2\pi^2\overline{\Delta\rho^2}$ were calculated as a measure of SAXS contrast $\overline{\Delta\rho^2}$ by trapezoidal integration of the model curves in the fit range (0.018 to 0.42 $Å^{-1}$). In the SRO phase, the typical interparticle distance of nearest neighbors was calculated as $d_{nn,SRO} = \sqrt[3]{\frac{\frac{4}{3}\pi r_{eff}^3}{\eta}}$, where r_{eff} is the effective radius of the hard sphere interaction within the short-range ordered phase, and η is the volume fraction of the effectively interacting particles in this phase. In the fcc supercrystal, the nearest-neighbor distance is $d_{nn,fcc} = \frac{a}{\sqrt{2}}$, where a is the lattice constant of the cubic unit cell of the fcc assemblies as obtained from the fit of the peak positions. The surface-to surface separation was then calculated as $d = d_{nn} - 2R$, where $2R$ was obtained from the TS-PDF analysis and coincides with the diameter of a sphere fully enclosing the icosahedron.

Supporting Information

Supporting Information is available from the Wiley Online Library or from the author.

Acknowledgements

This work was partially supported by the Bundesministerium für Bildung und Forschung (BMBF) via the project 05K19GU7 / 05K19WMA (LUCENT I) and 05K22GU7 (LUCENT II), and Cluster of Excellence "CUI: Advanced Imaging of Matter" of the Deutsche Forschungsgemeinschaft (DFG)-EXC 2056-project ID 390715994 of the Deutsche Forschungsgemeinschaft, the ERC Consolidator Grant LINCHPIN (grant no. 818941), the Bavarian State Ministry of Science, Research and Arts through the grant "Solar Technologies go Hybrid (SolTech)". This research was carried out in part at PETRA III at the Deutsches Elektronen-Synchrotron DESY (Hamburg, Germany), a member of the Helmholtz Association (HGF), at the P07 beamline and was supported through the Maxwell computational resources. The authors greatly thank Mr. Stephan Fleig and the team of the Mechanical Workshop (Standortwerkstatt Bahrenfeld) of the University of Hamburg for their help in the realization of the in situ reactor. The authors would also like to thank Stefan Werner and Andrea Köppen for the collection of the TEM, HRTEM, and EDX data.

Open access funding enabled and organized by Projekt DEAL.

Conflict of Interest

The authors declare no conflict of interest.

Author Contributions

D.D. and K.F. contributed equally to this work. B.N. and D.K. supervised the project. D.D. and F.M. synthetized the nanocrystals, and D.D. carried out the characterization. D.D., K.F., B.N., D.K., O.G., and A-C.D. designed the simultaneous in situ X-ray scattering experiment and D.D., K.F., L.G., and B.N. carried out the relative measurements. K.F. performed the in-house SAXS measurements. D.D. analyzed the PDF data and K.F. the SAXS data. D.D., K.F., B.N., and D.K. wrote the manuscript. All authors discussed the results and commented on the manuscript.

Data Availability Statement

The data that support the findings of this study are openly available in [Zenodo] at [10.5281/zenodo.10138087].

Keywords

alloyed nanocrystals, oleic acid, oleylamine, PDF, SAXS, segregation, self-assembly

Received: December 15, 2023
Revised: February 20, 2024
Published online:

[1] a) S.-W. Hsu, A. L. Rodarte, M. Som, G. Arya, A. R. Tao, *Chem. Rev.* **2018**, *118*, 3100; b) I. Cherniukh, G. Rainò, T. Stöferle, M. Burian, A. Travesset, D. Naumenko, H. Amenitsch, R. Erni, R. F. Mahrt, M. I. Bodnarchuk, M. V. Kovalenko, *Nature.* **2021**, *593*, 535.

[2] a) C. R. Kagan, E. Lifshitz, E. H. Sargent, D. V. Talapin, *Science.* **2016**, *353*, aac5523; b) M. Hadjimichael, Y. Li, E. Zatterin, G. A. Chahine, M. Conroy, K. Moore, E. N. O. Connell, P. Ondrejkovic, P. Marton, J. Hlinka, U. Bangert, S. Leake, P. Zubko, *Nat. Mater.* **2021**, *20*, 495.

[3] a) H. Zhao, S. Sen, T. Udayabhaskararao, M. Sawczyk, K. Kučanda, D. Manna, P. K. Kundu, J.-W. Lee, P. Král, R. Klajn, *Nat. Nanotechnol.* **2016**, *11*, 82; b) W. Baek, M. S. Bootharaju, K. M. Walsh, S. Lee, D. R. Gamelin, T. Hyeon, *Nat. Mater.* **2021**, *20*, 650.

[4] M. R. Begley, D. S. Gianola, T. R. Ray, *Science.* **2019**, *364*, eaav4299.

[5] a) J. Shi, Z. Xiao, N. Kamaly, O. C. Farokhzad, *Acc. Chem. Res.* **2011**, *44*, 1123; b) H. Zhou, M. Guo, J. Li, F. Qin, Y. Wang, T. Liu, J. Liu, Z. F. Sabet, Y. Wang, Y. Liu, *J. Am. Chem. Soc.* **2021**, *143*, 1846; c) Y. Shamay, J. Shah, M. Işık, A. Mizrachi, J. Leibold, D. F. Tschaharganeh, D. Roxbury, J. Budhathoki-Uprety, K. Nawaly, J. L. Sugarman, *Nat. Mater.* **2018**, *17*, 361.

[6] a) M. V. Kovalenko, L. Manna, A. Cabot, Z. Hens, D. V. Talapin, C. R. Kagan, V. I. Klimov, A. L. Rogach, P. Reiss, D. J. Milliron, *ACS Nano.* **2015**, *9*, 1012; b) K. S. Sugi, A. Maier, M. Scheele, *Chem. Commun.* **2022**, *58*, 6998; c) C. Jenewein, S. M. Schupp, B. Ni, L. Schmidt-Mende, H. Cölfen, *Small Science.* **2022**, *2*, 2200014; d) I. Coropceanu, E. M. Janke, J. Portner, D. Haubold, T. D. Nguyen, A. Das, C. P. N. Tanner, J. K. Utterback, S. W. Teitelbaum, M. H. Hudson, N. A. Sarma, A. M. Hinkle, C. J. Tassone, A. Eychmüller, D. T. Limmer, M. Olvera de la Cruz, N. S. Ginsberg, D. V. Talapin, *Science.* **2022**, *375*, 1422; e) M. A. Boles, M. Engel, D. V. Talapin, *Chem. Rev.* **2016**, *116*, 11220; f) H. Han, S. Kallakuri, Y. Yao, C. B. Williamson, D. R. Nevers, B. H. Savitzky, R. S. Skye, M. Xu, O. Voznyy, J. Dshemuchadse, L. F. Kourkoutis, S. J. Weinstein, T. Hanrath, R. D. Robinson, *Nat. Mater.* **2022**, *21*, 518.

[7] a) A. R. Tao, S. Habas, P. Yang, *Small.* **2008**, *4*, 310; b) R. Jin, C. Zeng, M. Zhou, Y. Chen, *Chem. Rev.* **2016**, *116*, 10346; c) Y. Xia, K. D. Gilroy, H. C. Peng, X. Xia, *Angew. Chem., Int. Ed.* **2017**, *56*, 60; d) P.-C. Chen, M. Liu, J. S. Du, B. Meckes, S. Wang, H. Lin, V. P. Dravid, C. Wolverton, C. A. Mirkin, *Science.* **2019**, *363*, 959; e) V. Mantella, L. Castilla-Amorós, R. Buonsanti, *Chem. Sci.* **2020**, *11*, 11394; f) N. Kar, M. McCoy, J. Wolfe, S. L. A. Bueno, I. H. Shafei, S. E. Skrabalak, *Nat. Synth.* **2024**, 175.

[8] a) J. Schlotheuber né Brunner, B. Maier, S. L. J. Thomä, F. Kirner, I. A. Baburin, D. Lapkin, R. Rosenberg, S. Sturm, D. Assalauova, J. Carnis, Y. Y. Kim, Z. Ren, F. Westermeier, S. Theiss, H. Borrmann, S. Polarz, A. Eychmüller, A. Lubk, I. A. Vartanyants, E. V. Sturm, *Chem. Mater.* **2021**, *33*, 9119; b) W. Han, Z. Lin, *Angew. Chem., Int. Ed.* **2012**, *51*, 1534; c) N. Vogel, M. Retsch, C.-A. Fustin, A. Del Campo, U. Jonas, *Chem. Rev.* **2015**, *115*, 6265; d) W. Wei, F. Bai, H. Fan, *Angew. Chem., Int. Ed.* **2019**, *58*, 11956.

[9] a) B. Abécassis, F. Testard, O. Spalla, *Phys. Rev. Lett.* **2008**, *100*, 115504; b) L. Wu, J. J. Willis, I. S. McKay, B. T. Diroll, J. Qin, M. Cargnello, C. J. Tassone, *Nature.* **2017**, *548*, 197; c) D. R. Nevers, C. B. Williamson, B. H. Savitzky, I. Hadar, U. Banin, L. F. Kourkoutis, T. Hanrath, R. D. Robinson, *J. Am. Chem. Soc.* **2018**, *140*, 3652; d) F. Nakagawa, M. Saruyama, R. Takahata, R. Sato, K. Matsumoto, T. Teranishi, *J. Am. Chem. Soc.* **2022**, *144*, 5871; e) F. Montanarella, Q. A. Akkerman, D. Bonatz, M. M. van der Sluijs, J. C. van der Bok, P. T. Prins, M. Aebli, A. Mews, D. Vanmaekelbergh, M. V. Kovalenko, *Nano Lett.* **2023**, *23*, 667.

[10] T. Kister, D. Monego, P. Mulvaney, A. Widmer-Cooper, T. Kraus, *ACS Nano.* **2018**, *12*, 5969.

[11] J. J. Calvin, A. S. Brewer, A. P. Alivisatos, *Nat. Synth.* **2022**, *1*, 127.

[12] a) S. Karthika, T. Radhakrishnan, P. Kalaichelvi, *Cryst. Growth Des.* **2016**, *16*, 6663; b) P. G. Vekilov, *Nanoscale.* **2010**, *2*, 2346.

[13] a) D. Pontoni, T. Narayanan, A. Rennie, *Langmuir.* **2002**, *18*, 56; b) B. Abécassis, F. Testard, O. Spalla, P. Barboux, *Nano Lett.* **2007**, *7*, 1723; c) J. Polte, R. Erler, A. F. Thunemann, S. Sokolov, T. T. Ahner, K. Rademann, F. Emmerling, R. Kraehnert, *ACS Nano.* **2010**, *4*, 1076; d) K. M. Jensen, M. Christensen, P. Juhas, C. Tyrsted, E. D. Bøjesen, N. Lock, S. J. Billinge, B. B. Iversen, *J. Am. Chem. Soc.* **2012**, *134*, 6785; e) L. Grote, C. A. Zito, K. Frank, A.-C. Dippel, P. Reisbeck, K. Pitala, K. O. Kvashnina, S. Bauters, B. Detlefs, O. Ivashko, *Nat. Commun.* **2021**, *12*, 4429; f) J. K. Mathiesen, J. Quinson, A. Dworzak, T. Vosch, M. Juelsholt, E. T. Kjær, J. Schröder, J. J. Kirkensgaard, M. Oezaslan, M. Arenz, *J. Phys. Chem. Lett.* **2021**, *12*, 3224; g) J. Li, F. L. Deepak, *Chem. Rev.* **2022**, *122*, 16911.

[14] a) T. Li, A. J. Senesi, B. Lee, *Chem. Rev.* **2016**, *116*, 11128; b) F. Montanarella, J. J. Geuchies, T. Dasgupta, P. T. Prins, C. van Overbeek, R. Dattani, P. Baesjou, M. Dijkstra, A. V. Petukhov, A. van Blaaderen, D. Vanmaekelbergh, *Nano Lett.* **2018**, *18*, 3675; c) I. Lokteva, M. Koof, M. Walther, G. Grubel, F. Lehmkuhler, *Small.* **2019**, *15*, 1900438; d) E. Marino, D. J. Rosen, S. Yang, E. H. R. Tsai, C. B. Murray, *Nano Lett.* **2023**, *23*, 4250; e) C. P. N. Tanner, J. K. Utterback, J. Portner, I. Coropceanu, A. Das, C. J. Tassone, S. W. Teitelbaum, D. T. Limmer, D. V. Talapin, N. S. Ginsberg, *ACS Nano.* **2024**, *18*, 5778.

[15] D. Derelli, F. Caddeo, K. Frank, K. Krötzsch, P. Ewerhardt, M. Krger, S. Medicus, L. Klemeyer, M. Skiba, C. Ruhmlieb, O. Gutowski, A. C. Dippel, W. J. Parak, B. Nickel, D. Koziej, *Angew. Chem., Int. Ed.* **2023**, *62*, 202307948.

[16] a) X. Yin, M. Shi, K. S. Kwok, H. Zhao, D. L. Gray, J. A. Bertke, H. Yang, *Nano Res.* **2018**, *11*, 3442; b) J. K. Mathiesen, E. D. Bøjesen, J. K. Pedersen, E. T. Kjær, M. Juelsholt, S. Cooper, J. Quinson, A. S. Anker, G. Cutts, D. S. Keeble, *Small Methods.* **2022**, *6*, 2200420.

[17] S. Banerjee, C. H. Liu, K. M. O. Jensen, P. Juhas, J. D. Lee, M. Tofanelli, C. J. Ackerson, C. B. Murray, S. J. L. Billinge, *Acta Crystallogr. A.* **2020**, *76*, 24.

[18] a) Q. Zhang, J. Xie, J. Yang, J. Y. Lee, *ACS Nano.* **2009**, *3*, 139; b) J. Reyes-Gasga, S. Tehuacanero-Nuñez, J. Montejano-Carrizales, X. Gao, M. Jose-Yacaman, *Top. Catal.* **2007**, *46*, 23; c) J. Reyes-Gasga, S. Tehuacanero-Nuñez, J. Montejano-Carrizales, *Acta Microsc.* **2009**, *18*, 304.

[19] a) M. Klokkenburg, J. Hilhorst, B. Erné, *Vib. Spectrosc.* **2007**, *43*, 243; b) N. Shukla, C. Liu, P. M. Jones, D. Weller, *J. Magn. Magn. Mater.* **2003**, *266*, 178.

[20] a) S. Mourdikoudis, M. Menelaou, N. Fiuza-Maneiro, G. Zheng, S. Wei, J. Pérez-Juste, L. Polavarapu, Z. Sofer, *Nanoscale Horiz.* **2022**, *7*, 941; b) M. C. Weidman, Q. Nguyen, D.-M. Smilgies, W. A. Tisdale, *Chem. Mater.* **2018**, *30*, 807; c) J. Borges, J. A. Ribeiro, E. M. Pereira, C. A. Carreira, C. M. Pereira, F. Silva, *J. Colloid Interface Sci.* **2011**, *358*, 626.

[21] a) M. C. Weidman, D.-M. Smilgies, W. A. Tisdale, *Nat. Mater.* **2016**, *15*, 775; b) B. De Nijs, S. Dussi, F. Smallenburg, J. D. Meeldijk, D. J. Groenendijk, L. Filion, A. Imhof, A. Van Blaaderen, M. Dijkstra, *Nat. Mater.* **2015**, *14*, 56; c) A. Lesaine, D. Bonamy, C. L. Rountree, G. Gauthier, M. Impéror-Clerc, V. Lazarus, *Soft Matter.* **2021**, *17*, 1589.

[22] a) R. Mondal, G. Kumaraswamy, *Mater. Adv.* **2022**, *3*, 3041; b) R. Rajamanickam, S. Kumari, D. Kumar, S. Ghosh, J. C. Kim, G. Tae, S. Sen Gupta, G. Kumaraswamy, *Chem. Mater.* **2014**, *26*, 5161.

[23] a) B. J. Alder, T. E. Wainwright, *J. Chem. Phys.* **1957**, *27*, 1208; b) P. N. Pusey, W. Van Megen, *Nature.* **1986**, *320*, 340.
[24] G. Ashiotis, A. Deschildre, Z. Nawaz, J. P. Wright, D. Karkoulis, F. E. Picca, J. Kieffer, *J. Appl. Crystallogr.* **2015**, *48*, 510.
[25] P. Juhás, T. Davis, C. L. Farrow, S. J. L. Billinge, *J. Appl. Crystallogr.* **2013**, *46*, 560.
[26] P. Juhás, C. L. Farrow, X. Yang, K. R. Knox, S. J. L. Billinge, in Acta Crystallographica Section A: Foundations and Advances, *71*, **2015**, 562.
[27] A. Hjorth Larsen, J. Jorgen Mortensen, J. Blomqvist, I. E. Castelli, R. Christensen, M. Dulak, J. Friis, M. N. Groves, B. Hammer, C. Hargus, E. D. Hermes, P. C. Jennings, P. Bjerre Jensen, J. Kermode, J. R. Kitchin, E. Leonhard Kolsbjerg, J. Kubal, K. Kaasbjerg, S. Lysgaard, J. Bergmann Maronsson, T. Maxson, T. Olsen, L. Pastewka, A. Peterson, C. Rostgaard, J. Schiotz, O. Schutt, M. Strange, K. S. Thygesen, T. Vegge, et al., *J Phys Condens Matter.* **2017**, *29*, 273002.
[28] M. Doucet, J. H. Cho, G. Alina, Z. Attala, J. Bakker, W. Bouwman, R. Bourne, P. Butler, I. Cadwallader-Jones, K. Campbell, T. Cooper-Benun, C. Durniak, L. Forster, P. Gilbert, M. Gonzalez, R. Heenan, A. Jackson, S. King, P. Kienzle, J. Krzywon, B. Maranville, R. Murphy, T. Nielsen, L. O'Driscoll, W. Potrzebowski, S. Prescott, R. Ferraz Leal, P. Rozyczko, T. Snow, A. Washington, et al., SasView version 5.0.5. Zenodo.
[29] R. O. Matt Newville, A. Nelson, T. Stensitzki, A. Ingargiola, D. Allan, A. Fox, F. Carter, R. O. Michał, D. Pustakhod, lneuhaus, S. Weigand, A. Aristov, C. D. Glenn, mgunyho, Mark, A. L. R. Hansen, G. Pasquevich, L. Foks, N. Zobrist, O. Frost, Stuermer, azelcer, A. Polloreno, A. Persaud, J. H. Nielsen, M. Pompili, P. Eendebak, **2023**. Imfit/lmfit-py: 1.2.2. Zenodo.

